

Rearrangement of dislocation structures in the aging of ice single crystals

V. Taupin^a, T. Richeton^{a,b}, J. Chevy^b, C. Fressengeas^{a,*}, J. Weiss^b,
F. Louchet^b, M.C. Miguel^c

^a *Laboratoire de Physique et Mécanique des Matériaux, Université Paul Verlaine – Metz/CNRS, Ile du Saulcy, 57012 Metz, Cedex, France*

^b *Laboratoire de Glaciologie et Géophysique de l'Environnement – CNRS, 54 rue Molière, 38402 Saint Martin d'Hères, Cedex, France*

^c *Departament de Física Fonamental, Facultat de Física, Universitat de Barcelona, Diagonal 647, 08028 Barcelona, Spain*

Received 11 July 2007; received in revised form 3 December 2007; accepted 3 December 2007

Available online 31 January 2008

Abstract

Aging of ice single crystals subjected to creep exhibits peculiar behavior. If the sample is unloaded after sufficient strain, a forward jump in creep rate is observed at reloading. Sequences of loading periods alternated with either increasing or decreasing unloading intervals were performed to document this phenomenon. During the tests, acoustic emission was recorded in order to characterize dislocation activity and spatial distribution. Predictions obtained from a field dislocation theory coupling the evolution of statistical and polar dislocation densities compare fairly well with experimental results. Polar dislocation density reflects lattice incompatibility and long-range internal stresses. The associated back-stress and its relaxation during aging are seen as the origin of the acceleration effect. The interplay between dislocation velocity enhancement and polar dislocation annihilation during aging controls the phenomenon, whereas statistical dislocations only play a minor role. The reverse relaxation deformation observed during unloading periods is reproduced well by the model.

© 2007 Acta Materialia Inc. Published by Elsevier Ltd. All rights reserved.

Keywords: Ageing; Compression test; Dislocation dynamics; Self-organization and patterning; Strain gradient plasticity

1. Introduction

In crystalline materials, aging of the microstructure may be driven by creep or diffusion. Examples are grain growth, recrystallisation and recovery, processes via which dislocations rearrange under stress into structures involving lower levels of elastic strain energy. In strained solid solutions, diffusion of solute atoms to dislocations temporarily arrested at their obstacles is responsible for static and dynamic strain aging, processes which are at the origin of spectacular instabilities of plastic flow in metals known as Lüders bands and jerky flow or the Portevin–Le Chatelier effect, respectively. In ice single crystals, microstructural evolution associated with aging occurs by rearrangement

of dislocation ensembles only. Yet, as shown below, aging of ice single crystals subjected to creep can display paradoxical behavior: if the sample is unloaded for some time after sufficient strain, the creep rate exhibits a forward jump at reloading. In the following, we strive to understand this phenomenon in relation to features of dislocation transport and long-range internal stresses.

Ice is a hexagonal close packed (hcp) material with a strong anisotropy of slip. It deforms almost exclusively by dislocation glide on basal planes [1], and is characterized by a low Peierls stress [2]. Anisotropy and low lattice friction favor long-range elastic stresses and dislocation transport, as well as their interactions. Creep experiments using load increments also reveal that directional (kinematic) hardening associated with long-range elastic stress fields prevails over isotropic hardening originating in short-range interactions between dislocations [1]. Our working hypothesis

* Corresponding author. Tel.: +33 3 87 31 53 68; fax: +33 3 87 31 53 66.
E-mail address: claude.fressengeas@univ-metz.fr (C. Fressengeas).

is that the aging of dislocation structures is strongly coupled with their long-range stress field, and the purpose of this work is to investigate the influence of the aging time on the collective behavior of dislocation ensembles. With this aim, experimental data on torsion creep of ice single crystals at $-20\text{ }^{\circ}\text{C}$ and compression creep at $-10\text{ }^{\circ}\text{C}$, with sequences of either increasing or decreasing aging time between consecutive loading periods, are presented. Acoustic emission was recorded during the compression experiments in order to ascertain the spatiotemporal organization of plastic activity. The observations show that the distribution in space of plastic activity is inhomogeneous, even under carefully applied homogeneous external loading, which reveals long-range internal stress fields. An interpretation of the experimental results is pursued by using a field dislocation theory, which couples the dynamics of statistical and polar dislocation densities [3,4]. Polar dislocation densities (or “geometrically necessary dislocation” densities) are regarded as a continuous manifestation of lattice incompatibility. They are associated with the development of lattice curvature and long-range internal stress fields [5]. In contrast, statistical dislocations (or “statistically stored dislocations”) result in compatible deformation. Their individual stress fields statistically offset each other to a net zero overall stress field. Then short-range interactions prevail, which results in statistical forest hardening. Of course, there is no difference in nature between these two dislocation species, only a difference in the scale of resolution, as we recall below. In conventional (local) plasticity theories, only statistical dislocations are considered. Both species contribute to plastic flow, however. Their dynamics are coupled, because spatial gradients in the plastic distortion field due to statistical dislocations may generate polar dislocations. Approaches similar in spirit to the present model include those in Refs. [6,7,8,9,10]. The paper is organized as follows: Section 2 presents experimental data on the aging of ice single crystals obtained during sequential creep in torsion and compression, including acoustic emission measurements in compression. In Section 3, the field dislocation theory [3,4] and a one-dimensional (1-D) simplified version designed for compression are exposed. Results from the 1-D model are discussed in comparison with experiments in Section 4. Summary and conclusions follow.

2. Experimental

We carried out torsion and uniaxial compression creep experiments on cylindrical ice single crystals. Three crystals were crept, two under compression, and one under torsion. The crystals were grown from distilled, deionized and degassed water. They grew inside a cylindrical mould frozen at $0\text{ }^{\circ}\text{C}$ from the bottom in about one month, from a single crystal seed with the *c*-axis normal to the mould axis. The compression samples were cut such that basal planes, i.e. the preferred slip planes in hexagonal ice, were inclined at an angle less than 10° to the compression axis in test A

and 20° in test B. The sample diameter and height were 55 and 90 mm, respectively. With such orientation and sample dimensions, slight inhomogeneities in compressive loading, e.g. surface defects of ice–platen interfaces, are likely to induce gradients in dislocation distribution in the bulk of the sample, due to slip anisotropy. Indeed, similar to torsion or bending, compression has been shown to promote gradients in plastic strain, even in multi-slip *Al* [12]. However, no kink band was observed in our samples, which suggests proper application of boundary conditions. Several arguments further supporting this interpretation are presented below. The torsion sample diameter and height were 43 mm, and the torsion axis was orthogonal to the basal planes. The initial dislocation density (mostly sessile) inferred from synchrotron X-ray diffraction measurements conducted in similar crystals is low: $\rho_s \cong 10^8\text{ m}^{-2}$ [13]. Consequently the mean dislocation-to-dislocation distance amounts to $\rho_s^{-1/2} \cong 100\text{ }\mu\text{m}$. The compression experiments consisted in a sequence of loading and unloading periods (Fig. 1). First increased step by step over a period of 200 min, the load was kept constant during the loading steps (creep), then abruptly turned off and maintained to zero during the aging time, then abruptly turned on again for an identical loading step. For test A, the loading step duration was $t_l=30\text{ min}$ and the aging time t_w between loading periods was increased in the course of the test. The consecutive values were $t_w=1, 10, 100$ and 1000 min . For test B, the loading time was $t_l=60\text{ min}$, and the aging time t_w was decreased, with successive values $1000, 100, 10$ and 1 min . The macroscopic compression strain was measured during the loading steps, as well as the reverse deformation during the unloading periods. The accuracy of the linear variable differential transformer (LVDT) displacement transducer is certainly better than $5\text{ }\mu\text{m}$. Using the central limit theorem, the accuracy of the velocity measurements depends on the number of points involved. In test A, there were 600 points defining time intervals of 600 s. Hence, the measured velocity is obtained from the average of 300 slopes computed from 300 couples of points distant of 300 s. The maximum error on a strain rate measurement is therefore: $(5\text{ }\mu\text{m} + 5\text{ }\mu\text{m}) / (90\text{ mm} \times 300\text{ s}) = 3.7 \times 10^{-7}\text{ s}^{-1}$ (90 mm is the height of the sample). Hence, an upper bound for the averaged strain rate shown in Fig. 6 is $3.7 \times 10^{-7} / \sqrt{300} = 2 \times 10^{-8}\text{ s}^{-1}$. For test B, time intervals are 1200 s, given a total of 1200 points. The same calculations give the estimate of $8 \times 10^{-9}\text{ s}^{-1}$ for the error.

Six piezoelectric transducers (frequency band 200–750 kHz) were fixed to the samples by melting/freezing. These sensors allowed localizing acoustic emission sources within the samples. Details about the acoustic emission measurement techniques can be found in Ref. [14]. Using similar experiments, previous work [15,16] showed that in the absence of micro-cracking (cracks can be easily detected due to ice transparency), acoustic emission is related to intermittent motion of dislocations in the form of avalanches. An analysis of the spatial organization of

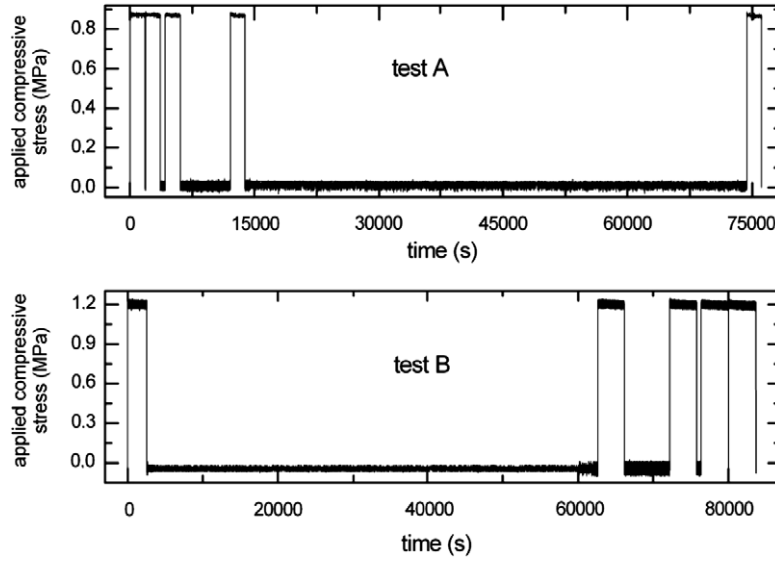


Fig. 1. Applied stress vs. time (temperature $-10\text{ }^{\circ}\text{C}$).

dislocation avalanches was performed during the loading periods in test A by means of a correlation integral analysis (see Ref. [17] for details). The analysis shows that avalanches are spatially correlated. Indeed, within a range limited at small scales by the spatial resolution threshold and at large scales by the sample diameter, scale-invariant spatial distributions of avalanche locations are observed with correlation dimension $D_c < 3$ (see Fig. 2). The value $D_c = 3$ would correspond to a perfectly random distribution. Accordingly, the non-uniform character of dislocation distributions is demonstrated. Moreover, it can be seen in Fig. 2 that the sooner the measurement is performed, the stronger the correlation. We therefore expect the existence of polar dislocation sources, due to gradients

in dislocation distribution, all the more so in the early stages of test A.

Figs. 3 and 4 show the evolution in time of the overall strain response during the loading steps in tests A and B. Two salient features are noticed as the sequences unfold, namely the evolution in size of the initial strain jump and that of the subsequent mean creep rate. The initial strain jump is much larger than the elastic response and, in both tests, it decreases with increasing aging time. However, the transient data should be considered with caution, as the methodology we used (manual control, low recording frequency and relatively low resolution of displacement sensors) was certainly not adequate for fast phenomena. The subsequent creep rate evolves rather slowly during the loading steps, although a small acceleration is observed followed by deceleration in the last loading steps, particularly so in test B. Its mean value increases from one loading step

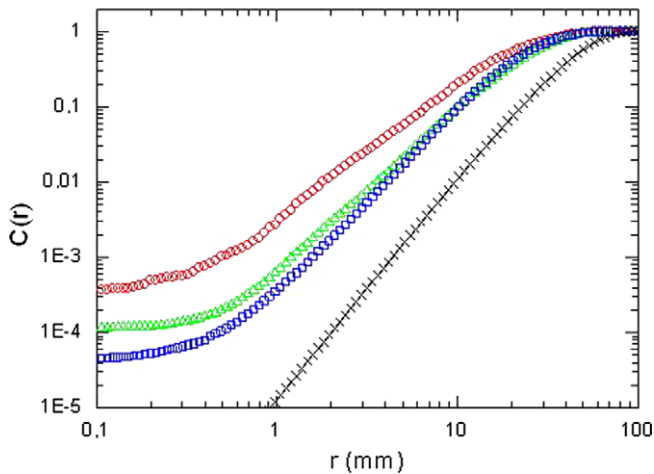


Fig. 2. Correlation integral analysis for the avalanche locations (test A). $C(r)$ is the probability of two locations being less than r apart. The scaling $C(r) \sim r^{D_c}$ is observed during loading steps. Circles: after $t_w = 1\text{ min}$, $D_c = 1.80 \pm 0.1$. Triangles: after $t_w = 10\text{ min}$, $D_c = 2.15 \pm 0.1$. Squares: after $t_w = 100\text{ min}$, $D_c = 2.42 \pm 0.1$. Crosses: similar analysis performed for randomly distributed locations (Poisson distribution), $D_c = 2.9 \pm 0.1$.

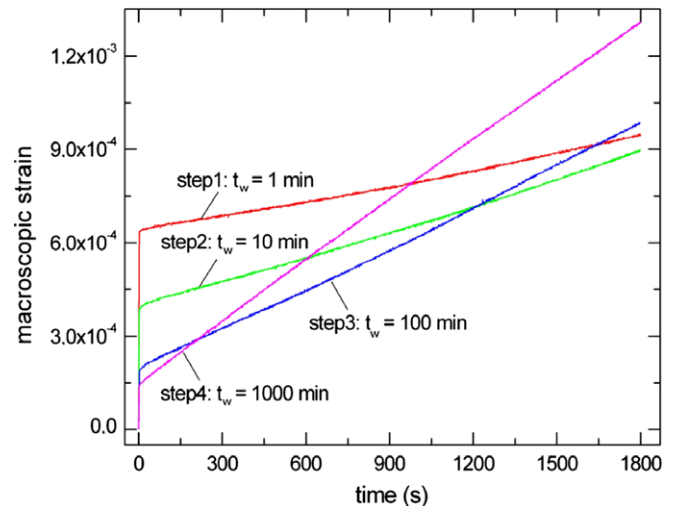


Fig. 3. Creep curves from the different loading steps of test A.

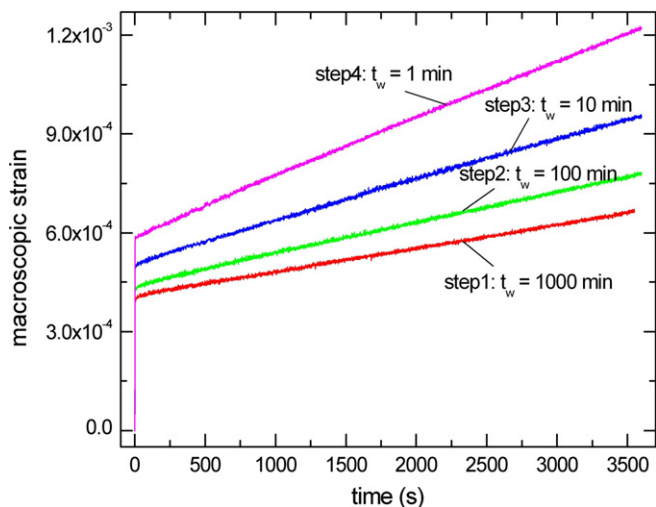


Fig. 4. Creep curves from the different loading steps of test B.

to the next one. This creep rate increase is qualitatively consistent with creep data reported in the literature for ice single crystals [18]. However, in addition to the well-documented continuous acceleration of creep, a strong jump forward in creep rate is observed when shifting from one loading step to the next (Figs. 6, 12). The order of magnitude (10^{-7} s^{-1}) of the jumps is much larger than the error on strain rate measurements ($2 \times 10^{-8} \text{ s}^{-1}$). Thus, the simple fact of unloading and reloading the crystal after some aging period increases the steady-state mean creep rate. This phenomenon cannot be attributed to offsets in the ice–platen interfaces initially supporting reloading by localized straining. Indeed, not only would the steady-state creep rate apparently increase in such circumstances, but the initial transient jump in strain would also increase, because it occurs before steady-state creep settles. However in test A, it does not, as Fig. 3 shows. Instead, it is correlated with the duration of the aging period, as mentioned above (see Figs. 3, 4). The reverse deformation observed during unloading periods in test A was small but measurable. In test B, it was virtually non-existent.

The torsion creep test was carried out using a similar sequence of loading and aging periods, with a smaller average shear stress ($\tau_a = 0.12 \text{ MPa}$). After a first loading step lasting 125 h, by the end of which the creep strain reaches 0.73, while remaining homogeneous, and a first aging period of 14.3 h, a 37% increase in creep rate was observed at reloading. The second loading step lasted 5 h, and was followed by aging for 4.8 h. Again the creep rate at reloading after aging (third loading step) increased by 31% with respect to the previous end-creep-rate. In addition to our previous arguments, the occurrence of the creep acceleration effect in torsion under different stress and temperature conditions strongly suggests that it is not an artefact of ill-applied boundary conditions, but instead that it originates in the interplay between aging and internal stress fields. We now explore such an interpretation by using a field dislocation theory.

3. A field dislocation theory using mesoscale phenomenology

The model uses the continuum description of dislocations based upon Nye’s dislocation density tensor α [19]. Operating on the normal \mathbf{n} to a unit surface S , α provides the net Burgers vector $\mathbf{b} = \alpha \mathbf{n}$ of all dislocations lines threading S , i.e. the incompatibility in plastic displacement found along the Burgers circuit surrounding this surface. When \mathbf{b} is zero because all individual Burgers vectors compensate statistically, the Nye tensor α is zero and all these dislocations are deemed “statistical”. For the same dislocation distribution, the characteristic size of the Burgers circuit, i.e. the scale of resolution of the dislocation ensemble, may be decreased to the point where only one dislocation line is threading surface S . Such a situation occurs when this characteristic size amounts to the mean dislocation-to-dislocation distance $\rho_s^{-1/2}$. Then α is certainly non-zero and the involved dislocation is labelled as a “polar dislocation”. More specifically, if \mathbf{b} is its Burgers vector, \mathbf{t} its line vector, then $\alpha = \mathbf{b} \otimes \mathbf{t}$. In the present problem, the resolution scale $\rho_s^{-1/2} \cong 100 \mu\text{m}$ is intermediate and the net Burgers vector is usually non-zero, although some of the dislocations threading S may statistically compensate and result in a null Burgers vector. The subscripts (i, j) in the density components α_{ij} then indicate the net Burgers vector and average line direction of the polar dislocations, respectively. The remaining statistical dislocations are not accounted for in Nye’s tensor. Due to the incompatibility in plastic displacement, the plastic distortion tensor \mathbf{U}_p is not a gradient. It has an incompatible part, \mathbf{U}_p^\perp , which results from the distribution α and is the solution to the incompatibility equation:

$$\text{curl } \mathbf{U}_p^\perp = -\alpha \quad (1)$$

written here at small strains [5]. Since the total displacement \mathbf{u} is integrable, \mathbf{U}_p^\perp is exactly offset by the incompatible part \mathbf{U}_e^\perp of the elastic distortion tensor. The compatible part, \mathbf{U}_e^\parallel , of this tensor is a gradient. At small strains, it is the difference between the displacement gradient $\mathbf{U} = \text{grad } \mathbf{u}$ and the compatible part of the plastic distortion, \mathbf{U}_p^\parallel . At the small scale of resolution where all dislocations are resolved, the total plastic distortion rate $\dot{\mathbf{U}}_p$ results from the motion of the polar dislocations α , with velocity \mathbf{V} (throughout this paper, a superposed dot indicates a time derivative). At the resolution scale used in the present problem ($100 \mu\text{m}$), statistical mobile dislocations are likely to be present. They contribute to the plastic distortion rate through the conventional plastic velocity gradient tensor \mathbf{L}_p . Then $\dot{\mathbf{U}}_p$ is [3,4]:

$$\dot{\mathbf{U}}_p = \alpha \times \mathbf{V} + \mathbf{L}_p \quad (2)$$

with dislocation velocity \mathbf{V} now averaged over S . The incompatible part of $\dot{\mathbf{U}}_p$ feeds the increment of polar dislocations through the transport equation for dislocation densities [11]:

$$\dot{\alpha} = -\text{curl } \dot{\mathbf{U}}_p \quad (3)$$

This equation, of hyperbolic character, is used as an evolution equation for polar dislocation densities. Through the **curl** of the total plastic distortion rate tensor $\dot{\mathbf{U}}_p$, it couples the polar and statistical dislocation densities in the nucleation of polar dislocations. The stress tensor \mathbf{T} is obtained from the tensor of elastic constants \mathbf{C}_e as

$$\mathbf{T} = \mathbf{C}_e : \{\mathbf{U}_e\} = \mathbf{C}_e : \{\mathbf{U}_e^{\parallel} + \mathbf{U}_e^{\perp}\} = \mathbf{C}_e : \{\mathbf{grad} \mathbf{u} - \mathbf{U}_p^{\parallel} - \mathbf{U}_p^{\perp}\} \quad (4)$$

where $\{\mathbf{A}\}$ denotes the symmetric part of tensor \mathbf{A} . It satisfies the equilibrium equation:

$$\mathbf{div} \mathbf{T} = 0 \quad (5)$$

Complementing the above equations with a constitutive relation for the average dislocation velocity \mathbf{V} as a function of stress and dislocation orientation, and with phenomenological evolution equations for statistical densities, one obtains a closed theory in the sense that it contains enough statements to derive uniquely the dynamics of stress and dislocation densities in some domain from boundary and initial conditions. Boundary conditions comprise the conventional stress and displacement conditions, as well as the specification of inward fluxes of dislocations. A more detailed account of this overarching framework can be found in [3,4]. The standard crystal plasticity framework is recovered when α is the null tensor, a condition often satisfied when the scale of resolution is commensurate to the (macroscopic) sample size. In this case, long-range interactions due to lattice incompatibility are overlooked. Conversely $\mathbf{L}_p = \mathbf{0}$ when all dislocations are resolved. For computational reasons, only small scale systems can then be solved. Owing to the macroscopic crystal size in the present problem and to the mean dislocation-to-dislocation distance (100 μm), a mixed approach where both α and \mathbf{L}_p are non-zero is appropriate [20]. Nevertheless, the numerical solution remains demanding in terms of computational resources. Let us now focus on compression loading. By restricting the attention to screw dislocations pertaining to a single slip system in the basal plane, say $(\mathbf{e}_1, \mathbf{e}_2)$, with Burgers vector oriented in a given direction, say \mathbf{e}_1 , and by assuming invariance by translation along the c -axis normal to this plane, a simplified model, still retaining the essential physical features, but much more tractable and suitable for parametric studies, can be derived from the above. The resulting equations are

$$\dot{\gamma} = \alpha_{11} v_2 + \rho_m b v \quad (6)$$

$$\dot{\alpha}_{11} = -\dot{\gamma}_{,2} \quad (7)$$

Here the stress is constant, b denotes the length of the Burgers vector, and a comma indicates a partial derivative. Eq. (6) expresses the shear strain rate $\dot{\gamma}$ in the glide plane as a function of polar screw and statistical dislocation mobility, while Eq. (7) stands for the nucleation of polar screw dislocations due to gradients in this mobility. Combining Eqs. (6) and (7), a 1-D transport equation with a source term is obtained:

$$\dot{\alpha}_{11} + (\alpha_{11} v_2)_{,2} = -(\rho_m b v)_{,2} \quad (8)$$

Such transport equations are encountered in various parts of physics, perhaps most notably in fluid dynamics. Here, it applies to the transport of dislocation densities and serves as our fundamental equation. In this relation, an account of the physics of dislocation velocity and of straining history is made through phenomenological statements. Following Ref. [1], we first assume a power-law relationship for the average polar and statistical dislocation velocities (v_2, v) in the form

$$v_2 = v = v_0 \text{sgn}(\sigma - \sigma_\mu) \left(\frac{|\sigma - \sigma_\mu|}{\sigma_0 + \sigma_h} \right)^2 \quad (9)$$

where σ is the constant creep stress, σ_μ is a back-stress and σ_h represents statistical hardening. Parameters (v_0, σ_0) are reference velocity and stress values, respectively. They are identified from the experimental data [1,2]. In these references, the velocity of individual dislocations increases linearly with stress, whereas the creep strain rate has exponent 2 in stress. Assuming rapid saturation of the mobile dislocation density, it follows from the Orowan equation that the average dislocation velocity varies approximately with the squared stress, as stated in relation (9). Isotropic statistical hardening is derived from the sessile density ρ_s in the Bailey–Hirsch form: $\sigma_h = \bar{\alpha} \mu b \sqrt{\rho_s}$, where μ denotes the elastic shear modulus and $\bar{\alpha}$ is a constant taken from previous calculations in torsion creep [20]. Only a fraction of the nucleated screws glides in the basal planes. They induce the back-stress σ_μ , with rate of formation:

$$\dot{\sigma}_\mu = \tilde{\alpha} \mu \alpha_{11} v_2 - \frac{|v_2|}{\hat{\alpha} b} \sigma_\mu \quad (10)$$

where $(\tilde{\alpha}, \hat{\alpha})$ are constants. Relation (10) is similar to the Armstrong–Frederick law for kinematic hardening [21], but here the back-stress builds up from polar dislocation mobility only. Note that the involved relaxation time $\tau = \hat{\alpha} b / |v_2|$ is inversely proportional to the polar dislocation velocity. It is such that, at equilibrium ($\dot{\sigma}_\mu = 0$), the back-stress value does not depend on the dislocation velocity, but only on the polar dislocation density. The complementary fraction of nucleated screw dislocations experiences out-of-plane motion due to non-Schmid components of stress arising from the internal stress field. Therefore the sessile density increases, due to the formation of edge segments by cross-slip in prismatic planes. Its rate of formation is assumed to be proportional to the rate of screw nucleation

$$\dot{\rho}_s = \frac{\beta}{b} |\dot{\alpha}_{11}| \quad (11)$$

Large β values reflect high probabilities of cross-slip, due to favorable crystal orientation. Similarly, large $\tilde{\alpha}$ values reflect the contribution to internal stresses of edge segments in the prismatic planes, in addition to polar screw dislocations in the basal planes. In all upcoming calculations, σ_h remains much smaller than the reference stress σ_0 , implying that statistical hardening is relatively insignificant, whereas

the back-stress σ_μ can be of the order of the applied stress. The mobile statistical dislocation density ρ_m has a very low initial value. It increases due to dislocation sources associated with edge jogs in prismatic planes [22]. Its nucleation rate is constant with coefficient C_1 . Saturation of mobile dislocations results from their mutual annihilation, with coefficient C_2 and saturation value C_1/b^2C_2 :

$$\dot{\rho}_m = \left(\frac{C_1}{b^2} - C_2\rho_m \right) |\dot{\gamma}| \quad (12)$$

Out-of-plane motion of dislocations and back-stress formation are built-in features of the complete 3-D model. Hence the latter involves phenomenological constants (C_1, C_2) only for the evolution of statistical mobile dislocations (12). Assuming invariance along the direction normal to the slip plane, the 1-D model loses these attributes. The introduction of the additional phenomenological relations (9)–(11) and constants ($\bar{\alpha}, \tilde{\alpha}, \hat{\alpha}, \beta$) is an offset for this simplification, for which consistency in the results in torsion creep [20] offers a justification. In the present work, only the 1-D model is used. All parameter values are given in Table 1 in the case of test A. As the applied shear stress is larger in test B, the cross-slip probability is higher since the out-of-plane component of the applied stress is larger (with consequences on ($C_1, C_2, \tilde{\alpha}, \beta$)), and the reference stress σ_0 and velocity v_0 are larger. As the differences are small, however, the explicit dependence on stress has not been formalized in the model, for the sake of simplicity. The constants ($C_1, C_2, \tilde{\alpha}, \beta$) are obtained from the best fit between experimental and predicted creep curve in Figs. 5 and 11. The relevance of the model will be shown in what follows by its ability to independently predict the anelastic relaxation strain. As already mentioned, boundary conditions are written in terms of dislocation fluxes. Inward flux of dislocations is not permitted, although dislocation sources on boundaries are allowed. Outward movement of dislocations is permitted without constraint. The initial dislocation density distributions are hardly known, and there is necessarily some arbitrariness in their choice. However, there are constraints in the procedure. First, these dislocation distributions need to be consistent with the experimental initial strain rate according to Eq. (6). Second, they must lie in the range of usually measured densities [13], and finally there must be some non-uniformity, as suggested by the acoustic emission measurements shown in Fig. 2. We conservatively assume a constant statistical distribution, a linear variation

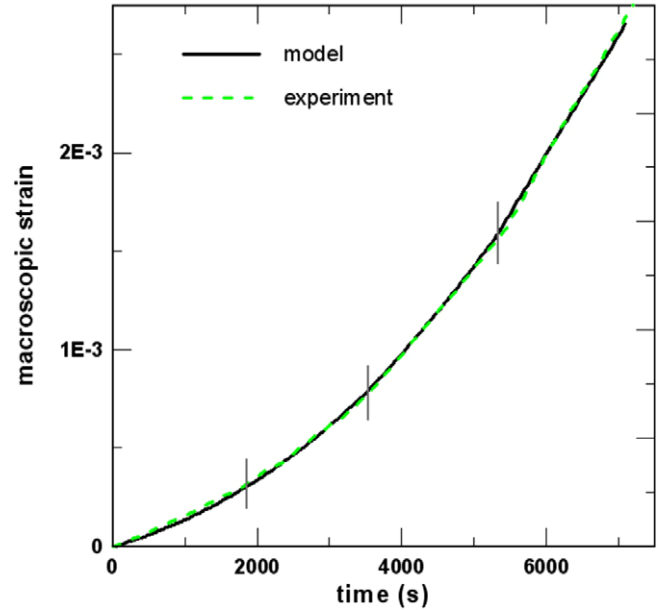


Fig. 5. Collection of stationary creep curves of test A; experiment and modeling. The vertical lines indicate the transition from one step to the next, and can be identified by a discontinuity in the strain rate. Reverse deformation during unloading periods is omitted.

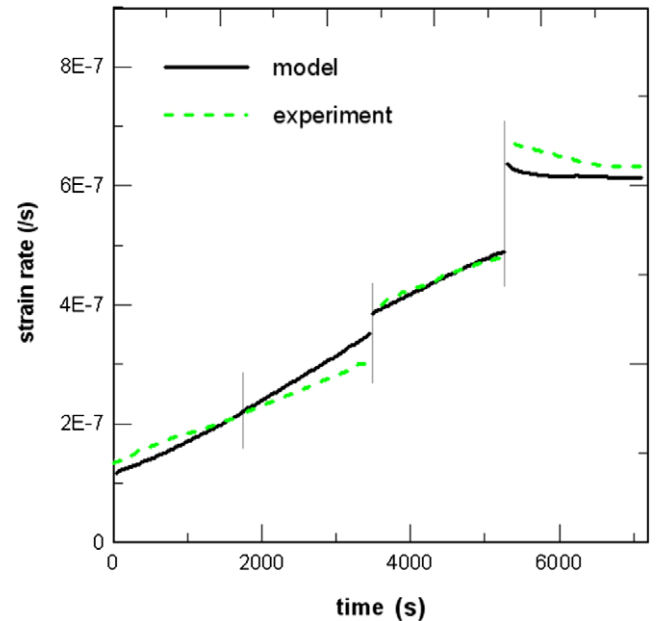


Fig. 6. Evolution of experimental and simulated strain rate during all loading steps in test A, derived from curves in Fig. 5. Unloading periods are omitted.

Table 1
Numerical constants used in the model (test A)

b	v_0	σ_0	
4.5×10^{-10} m	5.2×10^{-7} m s ⁻¹	0.135 MPa	
μ	$\bar{\alpha}$	$\tilde{\alpha}$	$\hat{\alpha}$
3GPa	0.133	1.2121	1.65×10^5
β	C_1	C_2	
0.3	4.9×10^{-7}	88.86	

of polar dislocation density, and adopt the values shown in Table 2 for test A as a best fit to satisfy these constraints.

Table 2
Initial conditions (test A)

ρ_m	ρ_s	α_{11}	σ_μ
3.75×10^9 m ⁻²	10^8 m ⁻²	0.031 m ⁻¹	-0.027 MPa

4. Results and discussion

Figs. 5 and 6 allow the creep curves obtained from simulations of test A to be compared with experimental data. The transient anelastic strain at reloading is not reproduced by the model, and is not under focus as its record might be dubious. Nevertheless, we believe that it might originate in mobile statistical dislocations being cleared away from the sample at reloading. Annihilation of part of these dislocations during the previous aging period would then explain its inverse correlation with aging time, but this conjecture cannot be checked from the model. Creep rate jumps at reloading after aging are retrieved, particularly after long aging periods (see Fig. 6), as well as the slight increase in steady-state creep rate and the hardening trend observed at large strains. Creep rate jumps result from a competition between two mechanisms related to back-stress build-up during loading periods and its relaxation during aging. On the one hand (see Fig. 7), back-stress relaxation leads to higher effective stress, and in turn to larger dislocation velocity, as implied by Eq. (9). This mechanism leads to larger strain rates at reloading. On the other hand, the direction of straining is reversed by the back-stress during aging. Throughout this period, polar dislocations formed during the previous loading period reverse their path, and polar dislocations of opposite sign nucleate and are transported forward. Therefore the structure of polar dislocations formed during the previous loading period is partially annihilated, as shown in Fig. 8. Reducing the polar dislocation density tends to lessen the strain rate at reloading, an opposite effect to that on dislocation velocity. The simulations revealed that in the interplay, the increase in dislocation velocity prevails over the annihilation

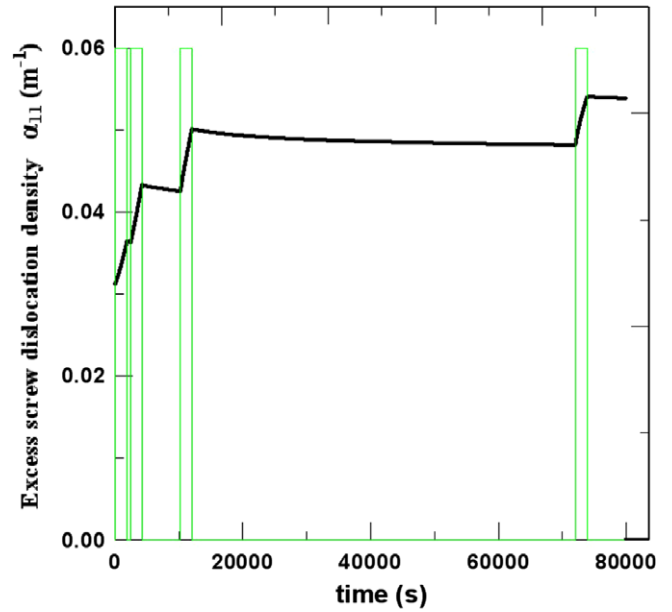


Fig. 8. Evolution of simulated average polar screw density during test A. The loading outline is indicated for clarity.

tion of polar dislocations, which entails higher creep rates at reloading. Note in Fig. 9 that, as statistical multiplication mechanisms are not sensitive to the straining direction, in contrast to polar dislocations, statistical mobile dislocation density increases during aging. These extra statistical mobile dislocations, although small in number, enhance the overall strain rate at reloading and the forward jump effect. The associated back-stress assumes high values before being significantly relaxed during long aging periods (see Fig. 7). This feature is consistent with the experimental correlation analysis shown in Fig. 2. Indeed, states of large

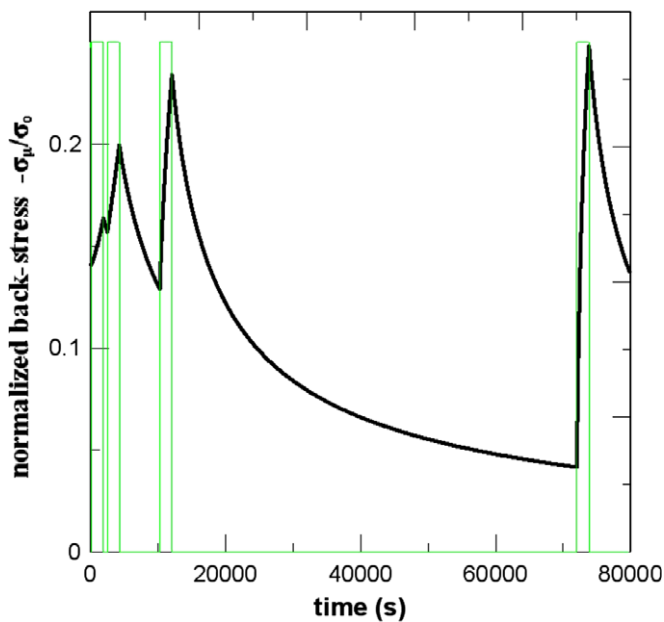


Fig. 7. Evolution of simulated average back-stress during test A. The loading stepped outline is indicated for clarity.

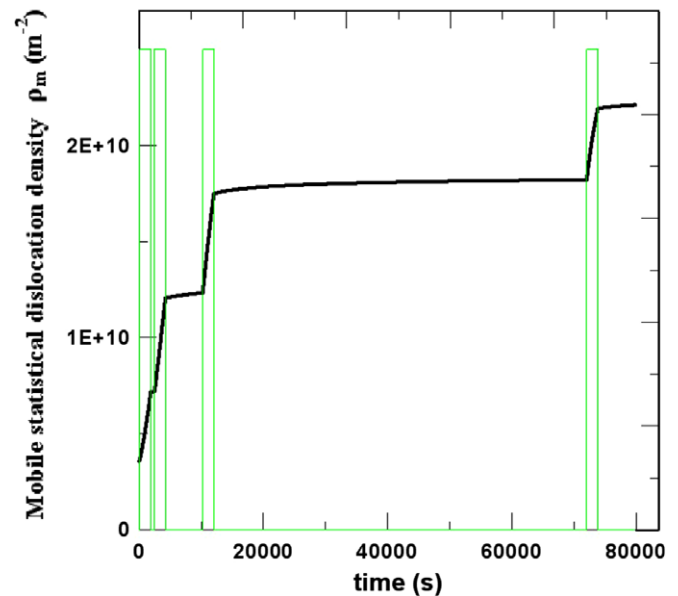


Fig. 9. Evolution of simulated mobile dislocation density during test A. The loading outline is indicated for clarity.

polar density are associated with high values of the correlation integral, while correlation weakening corresponds to the relaxation of these dislocation structures. The reverse relaxation deformation observed during unloading periods in test A is well reproduced by the model (see Fig. 10), which provides an indication of its predictive capabilities. According to the model, relaxation stems from the backward motion, driven by the back-stress, of the polar dislocations formed during the previous loading steps.

As mentioned above, test B shows similar trends (see Figs. 11, 12). However, as the applied stress is larger (see Fig. 1), the dislocation velocity is also larger and the nucleation of polar dislocations more effective. Hence, the back-stress reaches higher values, and it may become large enough to induce temporary hardening during the loading periods before polar dislocation nucleation prevails and softening takes over (see second and third stage of creep in Fig. 12). In the last creep stage of both tests A and B, hardening is even monotonic. Another consequence of the larger value of the applied stress is that the relaxation time τ can assume very short initial values. The relaxation of the back-stress then becomes very fast, which explains the near absence of reverse deformation during unloading, a feature fully retrieved by the model: the back-stress quickly becomes so small that it cannot drive the reverse motion of polar dislocations.

It is perhaps of interest to explain why we believe standard plasticity would be ineffective in the interpretation of the jump forward phenomenon. The present model involves dislocation transport and long-range internal stress fields. It has the ability to deal with situations where

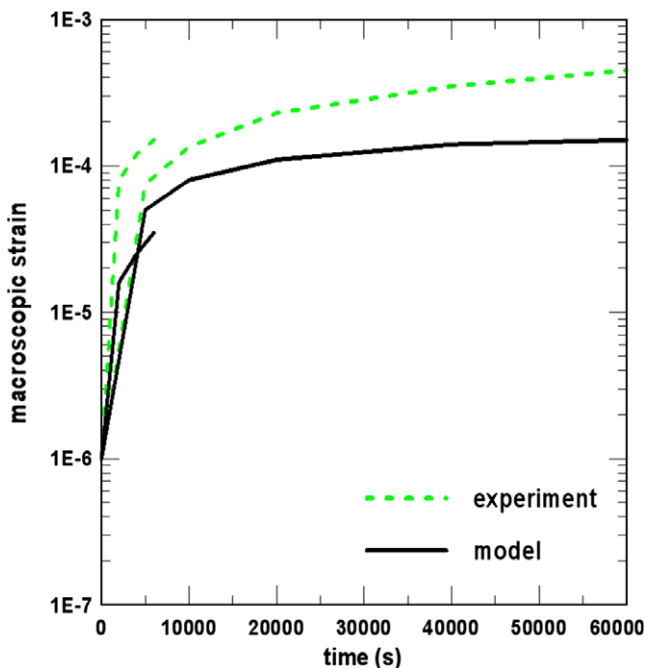


Fig. 10. Evolution of experimental and simulated reverse deformation during unloading periods (100 min and 1000 min) in test A.

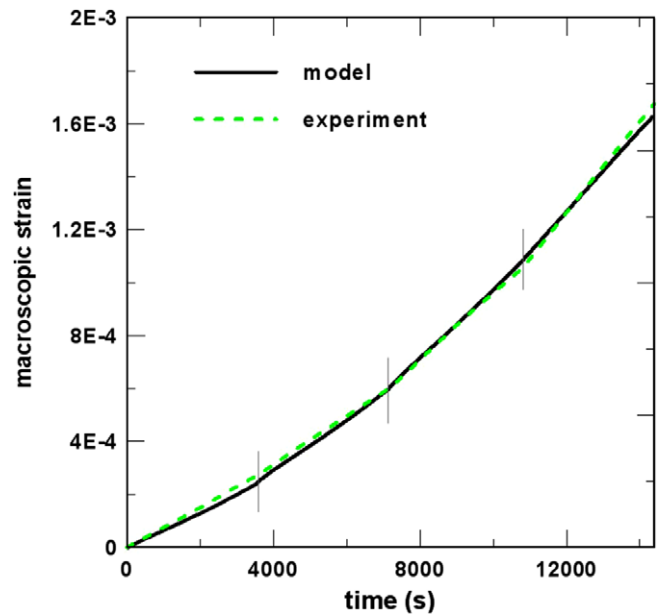


Fig. 11. Evolution of experimental and simulated strain during all loading steps for test B. Unloading periods are omitted.

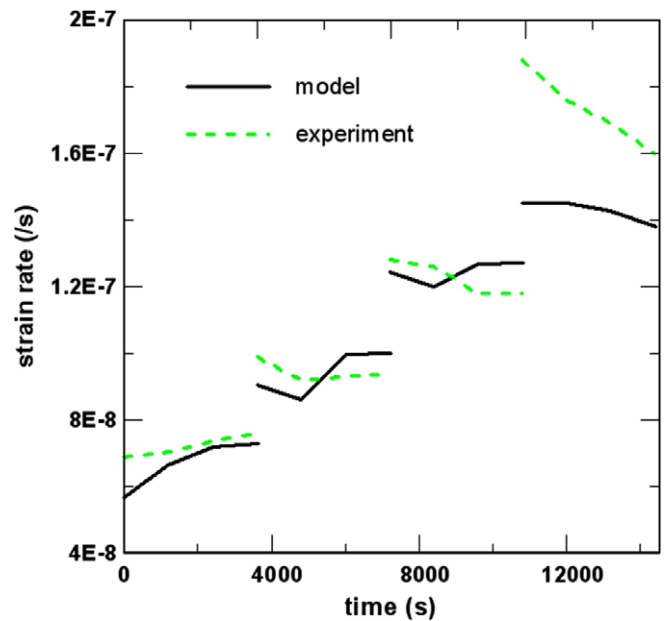


Fig. 12. Evolution of experimental and simulated strain rate during all loading steps for test B. Unloading periods are omitted.

directional hardening induced by internal stresses prevails over statistical hardening, like creep of ice single crystals. In its 1-D version, internal stresses are phenomenologically introduced in the description, as is customarily done in standard plasticity, through an Armstrong–Frederick-style equation for back-stress evolution. However, in contrast to standard plasticity treatment, the relevant constitutive equation (Eq. (10)) expresses the back-stress evolution in terms of polar dislocations only. Indeed statistical dislocations do not induce long-range internal stresses and should not contribute to back-stress build-up. In addition, the

proposed model deals separately with dislocation density and dislocation velocity, which, in contrast, are merged into plastic strain rate in standard plasticity treatment. This feature is consistent with common material science practice, which provides material data in terms of dislocation velocity and density [1, 2]. Further, it proves to be essential in the understanding of the jump forward phenomenon, as aging effects on dislocation velocity and dislocation density are actually competing each other. Finally, the experimental length scales (in the centimeter range) and time scales (in the 10^3 s range) are fully accounted for by the model, but would most likely preclude treatment by discrete dislocation dynamics simulation.

5. Summary and conclusions

The rearrangement of polar dislocations structures in the aging of ice single crystals and its influence on the creep rate has been discussed. A jump forward in the creep rate at reloading after aging has been evidenced in both torsion and compression creep under various stress and temperature levels. Due to its occurrence in various situations, this phenomenon cannot be interpreted in terms of localized imperfections of boundary conditions. Acoustic emission records reveal the existence of gradients in dislocation density distribution in compression samples, providing evidence for polar dislocation nucleation, lattice incompatibility and internal stresses. In torsion creep, the latter originate in gradients inherent to boundary conditions. Hence, a field dislocation mechanics approach accounting for lattice incompatibility and dislocation transport is proposed. Simulations based on the model are in fairly good agreement with experimental data in compression creep. The observed jump forward in the creep rate at reloading after aging is explained by the formation of polar dislocation structures during loading periods and their relaxation. The associated long-range stresses induce directional (kinematic) hardening and back-stress formation. On the one hand, back-stress relaxation during aging results in an increase of the effective stress and dislocation velocity at reloading. On the other hand, the back-stress reverses the direction of straining during aging, and polar dislocations of opposite sign nucleate. The latter annihilate with the existing polar dislocation structures. In terms of dislocation mobility and plastic strain rate, these two phenomena have

opposing effects. The simulations show that dislocation velocity enhancement prevails over dislocation annihilation. As a consequence, the overall creep rate jumps forward at reloading. Backward straining during aging induces a reverse (anelastic) relaxation deformation that is reproduced well by the model. Statistical dislocations, in particular those formed under back-stress loading during aging, reinforce the overall dislocation mobility and enhance the acceleration effect, but their contribution remains secondary.

Acknowledgement

We thank Profs. A.J. Beaudoin and A. Acharya for many inspiring discussions. M.C.M. acknowledges financial support from the Spanish Ministerio de Educación y Ciencia (HF2004-0062 and FIS2004-05923-C02) and Generalitat de Catalunya (Distinció).

References

- [1] Duval P, Ashby MF, Anderman I. *J Phys Chem* 1983;87:4066–74.
- [2] Shearwood C, Whitworth RW. *Phil Mag* 1991;64:289–302.
- [3] Acharya A, Roy A. *J Mech Phys Sol* 2006;54:1687–710.
- [4] Varadhan S, Beaudoin AJ, Fressengeas C. In: *Proc of Science 2006, SMPRI2005*, 004.
- [5] Kröner E. *Erg Angew Math* 1958;5:1–179.
- [6] Groma I. *Phys Rev B* 1997;56:5807–13.
- [7] El-Azab A. *Phys Rev B* 2000;61:11956–66.
- [8] Sedlacek R, Kratochvil J, Werner E. *Phil Mag* 2003;83:3735.
- [9] Zaiser M, Hochrainer T. *Scripta Mater* 2006;54:717–21.
- [10] Limkumnerd S, Sethna JP. *Phys Rev Lett* 2006;96:095503.
- [11] Mura T. *Phil Mag* 1963;89:843–57.
- [12] Nielsen SF, Poulsen HF, Beckmann F, Thorning C, Wert JA. *Acta Mater* 2003;51:2407–15.
- [13] Montagnat M, Duval P, Bastie P, Hamelin B. *Scripta Mater* 2003;49:411–5.
- [14] Richeton T, Weiss J, Louchet F. *Acta Mater* 2005;53:4463–71.
- [15] Weiss J, Grasso JR. *J Phys Chem* 1997;B 101:6113–7.
- [16] Miguel MC, Vespignani A, Zapperi S, Weiss J, Grasso JR. *Nature* 2001;410:667–71.
- [17] Weiss J, Marsan D. *Science* 2003;299:89–92.
- [18] Hobbs PV. *Ice physics*. Oxford: Oxford University Press; 1974.
- [19] Nye JF. *Acta Metall* 1953;1:153–62.
- [20] Taupin V, Varadhan S, Chevy J, Fressengeas C, Beaudoin AJ, Montagnat M, et al. *Phys Rev Lett* 2007;99:155507.
- [21] Armstrong PJ, Frederick CO. A mathematical representation of the multiaxial Bauschinger effect. Technical Report RD/B/N/731, Central Electricity Generating Board (1966).
- [22] Louchet F. *C.R., Physique* 2004;5:687–98.